Geophysical Journal International

Geophys. J. Int. (2021) **225,** 1952–1962 doi: 10.1093/gji/ggab069
GJI Gravity, Geodesy and Tides

Moho density contrast in Antarctica determined by satellite gravity and seismic models

M. Abrehdary [1] and L. E. Sjöberg [1,2]

[1] *Division of Mathematics, Computer and Surveying Engineering, University West (HV), SE-46186 Trollhättan, Sweden. E-mail: majabr@hv.se*
[2] *Division of Geodesy and Satellite Positioning, Royal Institute of Technology (KTH), SE-10044 Stockholm, Sweden*

Accepted 2021 February 16. Received 2020 November 18; in original form 2020 July 15

SUMMARY

As recovering the crust–mantle/Moho density contrast (MDC) significantly depends on the properties of the Earth's crust and upper mantle, varying from place to place, it is an oversimplification to define a constant standard value for it. It is especially challenging in Antarctica, where almost all the bedrock is covered with a thick layer of ice, and seismic data cannot provide a sufficient spatial resolution for geological and geophysical applications. As an alternative, we determine the MDC in Antarctica and its surrounding seas with a resolution of $1^\circ \times 1^\circ$ by the Vening Meinesz-Moritz gravimetric-isostatic technique using the XGM2019e Earth Gravitational Model and Earth2014 topographic/bathymetric information along with CRUST1.0 and CRUST19 seismic crustal models. The numerical results show that our model, named HVMDC20, varies from 81 kg m^{-3} in the Pacific Antarctic mid-oceanic ridge to 579 kg m^{-3} in the Gamburtsev Mountain Range in the central continent with a general average of 403 kg m^{-3}. To assess our computations, we compare our estimates with those of some other gravimetric as well as seismic models (KTH11, GEMMA12C, KTH15C and CRUST1.0), illustrating that our estimates agree fairly well with KTH15C and CRUST1.0 but rather poor with the other models. In addition, we compare the geological signatures with HVMDC20, showing how the main geological structures contribute to the MDC. Finally, we study the remaining glacial isostatic adjustment effect on gravity to figure out how much it affects the MDC recovery, yielding a correlation of the optimum spectral window ($7 \leq n \leq 12$) between XGM2019e and W12a GIA models of the order of $\sim$0.6 contributing within a negligible $\pm$14 kg m^{-3} to the MDC.

Key words: Antarctica; Gravity; Isostasy; Moho density contrast; uncertainty.

1 INTRODUCTION

The crust–mantle or Mohorovičić discontinuity (Moho) separates the Earth's crust from the upper mantle, with a density contrast, which traditionally was assumed to be of the order of 0.6 g cm^{-3} (e.g. Heiskanen & Moritz 1967, p. 135). Traditionally, the Moho depth (MD) is delineated from seismic data, such as active (controlled-source) seismic experiments using refracted or reflected seismic waves, passive methods based on seismic energy generated by earthquakes, receiver functions and the ambient noise technique (Laske *et al.* 2013 and Szwillus *et al.* 2019). The other Moho constituent, the Moho density contrast (crust–mantle density contrast or shortly MDC) can be estimated from the seismic signal velocity difference above and below the boundary converted to a density contrast. However, as seismic data collection is relatively costly, the data distribution is frequently sparse, in particular in Antarctica and over open seas.

With the advent of satellite gravity missions, it has been possible to image the MD and MDC via satellite gravity observations based on isostatic models. Such data allow more or less homogeneous coverage of the Earth by data (except for some restrictions in polar regions).

Although several authors have fairly well determined the MD by seismic or gravimetric techniques on global or regional scales, there are few studies specifically addressing the lithosphere density structure in Antarctica, where there is low spatial coverage of high-quality seismic data, which is the primary source of data for such studies. However, one can find some global MDC models derived from gravimetric or seismic experiments or combinations thereof. For instance, Sjöberg & Bagherbandi (2011) derived a method based on the Vening Meinesz-Moritz (VMM) technique and applied it globally in a model named KTH11, using gravity (EGM2008), topography (DTM2006) and seismic crust (CRUST2.0) data. Tenzer *et al.* (2012a) produced a global MDC

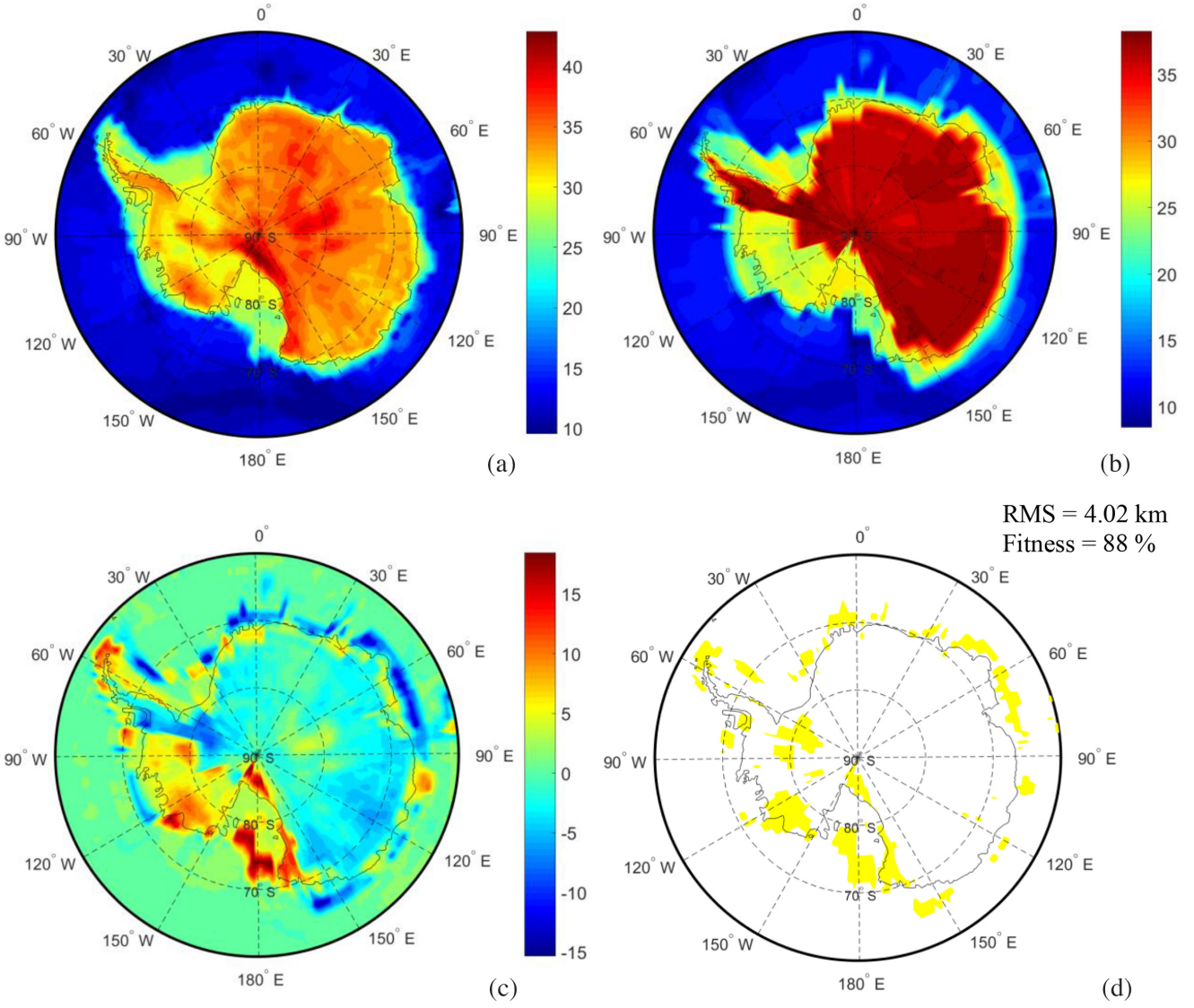

Figure 1. (a) MD derived by the CRUST1.0, (b) MD obtained from CRUST2.0, (c) differences between CRUST1.0 and CRUST2.0 MD and (d) coherence (or Fitness) between CRUST1.0 and CRUST2.0 MD model. Yellow pixels represent the grid cells where the hypothesis presented in eq. (9d) is rejected, that is, the two models are not consistent. RMS is root mean square of the difference between the two models.

model from EGM2008, DTM2008, CRUST2.0 and ICE-5G GIA models, differing about 7% from the global average of the MDC estimated by Sjöberg & Bagherbandi (2011). Tenzer *et al.* (2012b) demonstrated that the MDC under the oceanic crust is highly spatially correlated with the ocean-floor age, and Tenzer *et al.* (2013) argued that the MDC varies globally from 81.5 kg m^{-3} in the Pacific region to 988 kg m^{-3} beneath the Tibetan Plateau. Reguzzoni *et al.* (2013) estimated a global Moho model, named GEMMA12C, from the combination of the CRUST2.0 model and GOCE data, including both MD and MDC. Abrehdary *et al.* (2015) and (2017) presented two global Moho models using gravimetric data jointly with seismic data, containing both the MD and MDC and named them KTH14C and KTH15C. Abrehdary *et al.* (2019) estimated a new MDC model in ocean areas, using the marine gravity field from satellite altimetry in combination with a seismic crustal model and Earth's topographic/bathymetric data. The MDC can also be computed from the seismic crustal models CRUST2.0 (Bassin *et al.* 2000) and CRUST1.0 (Laske *et al.* 2013) as the difference between the densities in the upper mantle and lower crust.

Attempts for determining specifically the Antarctic MDC by gravimetric and seismic methods have also been published by some authors, such as Tenzer & Bagherbandi (2013), who employed the VMM technique with gravimetric data and constraining information from the global seismic crustal model CRUST2.0. Unfortunately, the crustal depths modelled by CRUST2.0 are poor in Antarctica, as we demonstrate in Section 3.2. Also, Llubes *et al.* (2018) estimated the crustal thickness in Antarctica and used a mean MDC of 0.63 g/cm^3 when adjusting the crustal thickness based on adding satellite gravimetric data to seismological results. Unfortunately, the error in assuming a constant MDC will significantly affect the gravimetric-isostatic estimation of the MD; see eq. (5) below. Pappa *et al.* (2019a) combined seismological and petrological models with satellite gravity gradient data to obtain the thermal and compositional structure of the Antarctic lithosphere. They also calculated the Antarctic MD by gravity inversion and found lower MDC in East

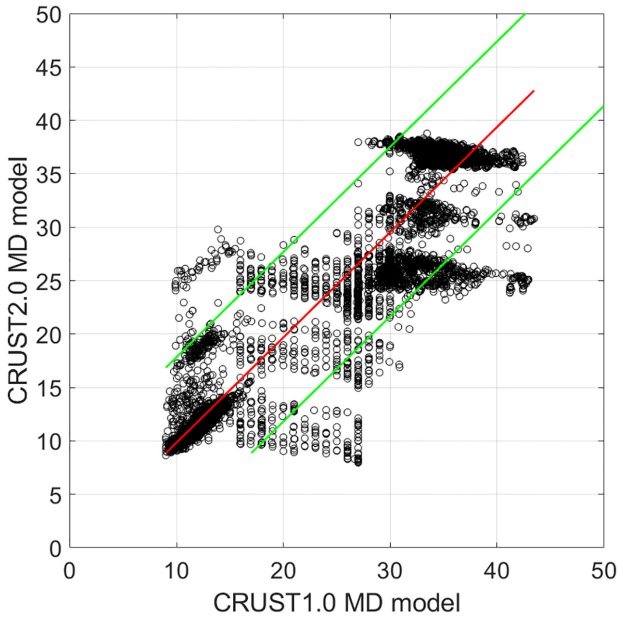

Figure 2. Scatter plots of the global MD models CRUST1.0 versus CRUST2.0.

Table 1. Statistics of global estimates of the gravity disturbances, stripping gravity corrections and NIEs. STD is the standard deviation of the estimated quantities in Antarctica. $\delta g^{\mathrm{FA}}_{\mathrm{XGM2019e}}$ is the free-air gravity disturbance provided by the XGM2019e. δg^{Topo}, δg^{Bath}, δg^{Ice} and δg^{Sedi} are the topographic/bathymetric, ice and sediment stripping gravity corrections derived from ESCM180. δg^{NIES} is the non-isostatic effect estimated by the CRUST19, and δg^{RFB} is the refined Bouguer gravity disturbance after applying the stripping gravity corrections and NIEs. Unit: mGal.

Unit	Quantities	Max.	Mean	Min.	STD
mGal	$\delta g^{\mathrm{FA}}_{\mathrm{XGM2019e}}$	86.20	− 7.28	− 74.92	21.17
	δg^{Topo}	43.06	− 193.45	− 487.45	162.77
	δg^{Bath}	576.51	280.22	157.71	142.51
	δg^{Ice}	325.78	104.37	4.61	97.10
	δg^{Sedi}	143.22	38.26	15	22.06
	δg^{NIEs}	161.61	− 107.97	− 376.44	78.24
	δg^{RFB}	424.47	-68.95	− 585.94	261.06

Antarctica versus West Antarctica without specifying in numbers (see Pappa *et al.* 2019b). Haeger *et al.* (2019) created a 3-D density, temperature, and composition model of the Antarctic lithosphere using an integrative approach combining gravity, topography and tomography data with mineral physics constraints and seismic data on crustal structures.

Here we produce a new MDC model (named HVMDC20) in Antarctica and its surroundings based on the VMM technique. We take advantage of the seismic models of CRUST19 (Szwillus *et al.* 2019) and CRUST1.0, the global topographic model Earth2014 (Hirt & Rexer 2015) and the free-air gravity data provided by the new Earth Gravitational Model XGM2019e (Zingerle *et al.* 2019). The output of this model is presented in five steps. The first step is to determine the MDC, the second step is to model the MDC uncertainty, the third step is to compare our estimates for MDC with previous seismic and gravimetric models and the last ones are to investigate the impact of the delayed glacial isostatic adjustment (GIA) on gravity and discuss relevant geodynamic processes occurring in the area.

2 METHODOLOGY

In this section, the MDC estimation is presented as a gravimetric-isostatic method. It implies that, the VMM problem is altered so that the Moho surface is known (e.g. from seismic data analysis), and the MDC is sought.

2.1 Vening Meinez-Moritz method

Our starting point is the following first-order global Fredholm integral equation for the MDC, denoted $\Delta\rho$, that satisfies the hypothesis of isostatic equilibrium, which yields a vanishing isostatic gravity disturbance $\delta g_I(P)$ for point P on the Earth's surface (*cf.* Sjöberg 2009, 2013):

$$R \iint_{\sigma} \Delta\rho K(\psi, s)\, \mathrm{d}\sigma = f(P), \tag{1a}$$

where σ is the unit sphere, R is mean Earth radius,

$$K(\psi, s) = \sum_{n=0}^{\infty} \frac{n+1}{n+3} \left(1 - s^{n+3}\right) P_n(\cos\psi), \tag{1b}$$

is the kernel function expressed by a series of Legendre's polynomials $P_n(\cos\psi)$ with ψ being the geocentric angle between the integration point and computation point P, $s = 1 - \tau = 1 - D/R$, D being the MD (at the integration point) and

$$f(P) = -\frac{1}{G}\left[\delta g_{\mathrm{B}}(P) + A_{\mathrm{C0}}(P)\right]. \tag{1c}$$

Here $\delta g_{\mathrm{B}}(P)$ is the Bouguer gravity disturbance corrected for the gravitational contributions of topography/bathymetry and crustal density variations of the oceans, ice and sediments. A_{C0} is the compensation attraction for a 'normal' Moho surface (mean MD in the target region) at depth D_0 below sea level and G is the gravitational constant. As we will see below, neither the constant A_{C0} nor lower degree spherical harmonics of the gravity disturbance are used in the calculations, as they do not contribute to the isostatic balance.

2.2 Solution for a variable MDC by spherical harmonics

The left-hand side of the integral of eq. (1a) was expanded in spherical harmonics (Y_{nm}) to second order by Sjöberg & Bagherbandi (2011), yielding

$$\begin{aligned} &R \iint_{\sigma} \Delta\rho K(\psi, s)\, \mathrm{d}\sigma \\ &= 4\pi \sum_{n=0}^{\infty} \sum_{m=-n}^{n} \tfrac{n+1}{2n+1} \left[(\Delta\rho D)_{nm} - \tfrac{n+2}{2R}\left(\Delta\rho D^2\right)_{nm}\right] Y_{nm}, \end{aligned} \tag{2}$$

and by also expressing the right-hand side of eq. (1a) as a harmonic series

$$f(P) = \sum_{n=0}^{\infty} \sum_{m=-n}^{n} f_{nm} Y_{nm}(P), \tag{3}$$

one obtains the spectral equation

$$\frac{4\pi(n+1)}{2n+1}[\,] = f_{nm} \quad \text{or} \quad [\,] = \frac{2n+1}{4\pi(n+1)} f_{nm}, \tag{4}$$

where the bracket is the same as in eq. (2). By summing up the spectral components, one thus arrives at the following solution for the product $D\Delta\rho$:

$$(D\Delta\rho)_P = \sum_{n=0}^{\infty} \sum_{m=-n}^{n} \left[\frac{2n+1}{4\pi(n+1)} f_{nm} + \frac{n+2}{2} \frac{\left(\Delta\rho D^2\right)_{nm}}{R}\right] Y_{nm}(P). \tag{5}$$

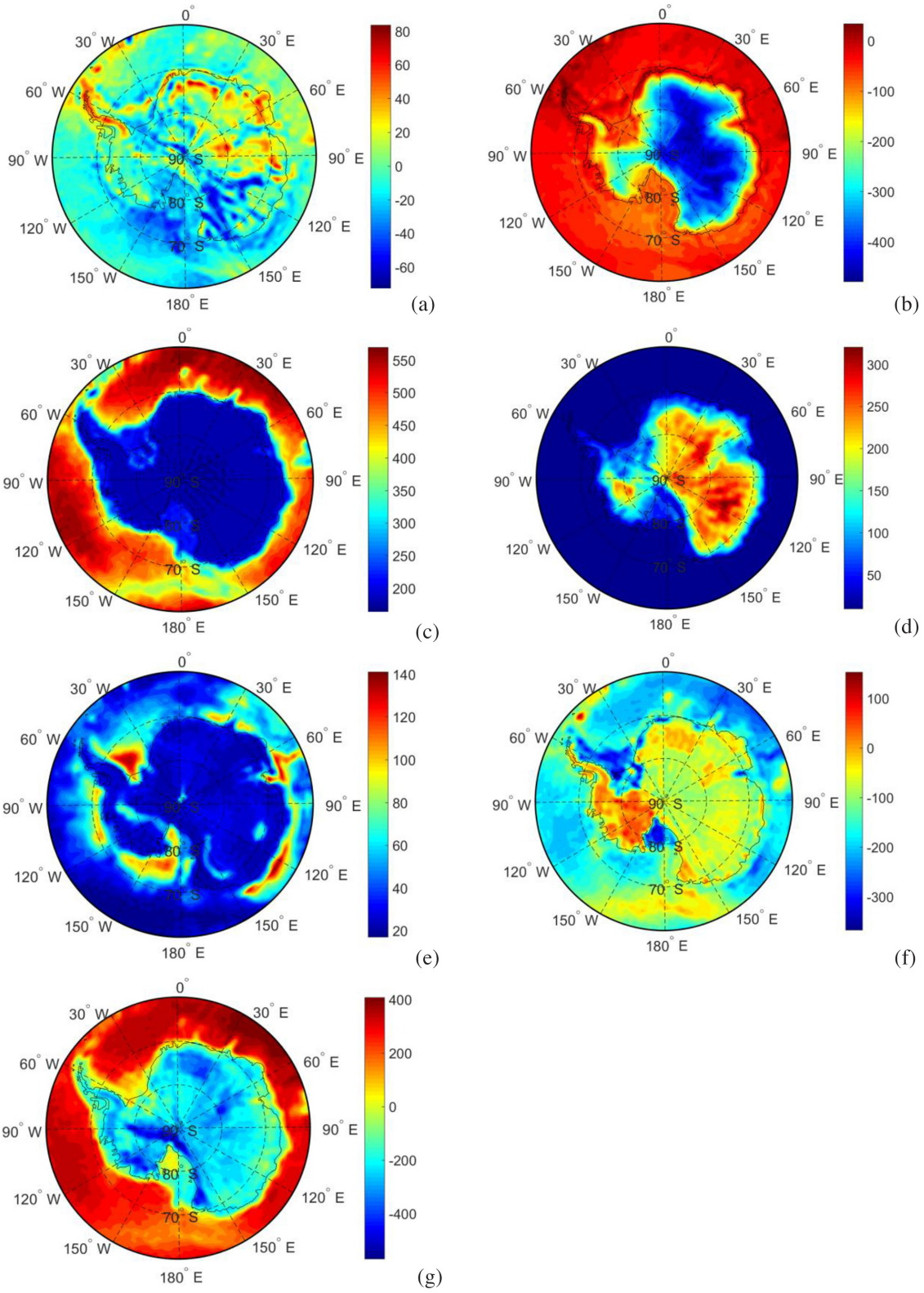

Figure 3. (a) The free-air gravity disturbances produced by the XGM2019e; (b) the topographic gravity correction; (c) the bathymetric gravity correction; (d) the ice density variation gravity correction; (e) the sediment density variation gravity correction; (f) the NIEs on gravity disturbance; and (g) the refined Bouguer gravity disturbances (in mGal).

Table 2. Statistics of the MDC and its uncertainty estimated from HVMDC20 model. STD is the standard deviation of the estimated quantities beneath Antarctic. $\Delta\rho^{\mathrm{HVMDC20}}$and $\sigma_{\Delta\rho^{\mathrm{HVMDC20}}}$ are the MDC and its uncertainty estimated from HVMDC20 model.

Unit	Quantities	Max.	Mean	Min.	STD
kg m^{-3}	$\Delta\rho^{\mathrm{HVMDC20}}$	579.05	402.98	80.98	122.98
	$\sigma_{\Delta\rho^{\mathrm{HVMDC20}}}$	83.97	19.52	0.28	14.66

By further using the approximation $\Delta\rho D^2/R \approx \Delta\rho D D_0/R$ (see Eshagh 2017), where D_0 is the mean MD over the study area, one obtains after a few manipulations the following second-order solution for the MDC for a known MD and omitting terms of degree higher than $n_{\max}$:

$$\Delta\rho(P) \approx \frac{1}{4\pi D}\sum_{n=0}^{n_{\max}}\sum_{m=-n}^{n}\frac{2n+1}{n+1}\left[1+\frac{D_0}{R}\frac{1}{2/(n+2)-D_0/R}\right]f_{nm}Y_{nm}(P) \tag{6a}$$

or

$$\Delta\rho(P) \approx \frac{f(P)}{2\pi D}-\frac{1}{4\pi D}\sum_{n=0}^{n_{\max}}\sum_{m=-n}^{n}\left[\frac{1}{n+1}-\frac{D_0/R}{2/(n+2)-D_0/R}\right]f_{nm}Y_{nm}(P). \tag{6b}$$

2.3 MDC uncertainty

Assuming there are no gross errors/blunders, the uncertainty of the MDC is composed of random and systematic errors, which can be expressed by the mean square error (Sjöberg & Bagherbandi 2011):

$$\mathrm{MSE}(\Delta\rho) = \sigma^2_{\Delta\rho} + \mathrm{bias}^2(\Delta\rho), \tag{7}$$

where $\sigma^2_{\Delta\rho}$ is the variance of the estimator of eq. (6a) or (6b) and the bias term consists of all contributions of systematic errors. As eqs (6a) and (6b) are based on the VMM method, it implies that any gravity signal that is not related with isostatic balance will cause a bias. Unfortunately, as no systematic error in this study is known, the only quality indicator we have in access is the standard error (STE), which is obtained by error propagation of the uncorrelated observation variances σ^2_f and σ^2_D (*cf.* Sjöberg & Bagherbandi 2011):

$$\sigma_{\Delta\rho} = \frac{1}{D_0}\sqrt{\sigma^2_f + \frac{\sigma^2_D f^2}{D_0^2}}. \tag{8}$$

As for the MD and its standard error provided by CRUST19, the problem is quite simple since the expected accuracy has already been computed by Szwillus *et al.* (2019), which we use in the present work.

3 NUMERICAL STUDIES

We will first describe the source of data to be used in the MDC determination (Section 3.1), followed in Section 3.2 by validation of CRUST1.0 versus CRUST2.0 and in Section 3.3 by the estimation of the MDC by assuming that the MD is known from the seismic Moho model CRUST19, and the section ends with estimating the MDC uncertainty. In Section 3.4, we compare the new MDC estimates with those of some other gravimetric-isostatic and seismic models (KTH11, GEMMA12C, CRUST1.0 and KTH15C).

3.1 Data sets

We employ the VMM model to image the MDC over Antarctica for both land and ocean areas. To reach this purpose, different data sets have been used, including the global Earth gravity field model (XGM2019e), the global topography model (Earth2014), and the global seismic crustal model (CRUST1.0 and CRUST19). In details, free-air gravity disturbances extracted from the XGM2019e global gravity field model in a set of $1^\circ \times 1^\circ$ blocks over Antarctic and surrounding are used. XGM2019e is a combined global gravity field model represented through spherical harmonics, which we will use up to degree and order $n_{\max}$ =180, corresponding to a spatial resolution of about 100 km, the approximate lower spatial limit for isostatic balance of the crust. The free-air gravity disturbances are applied to calculate the refined Bouguer gravity disturbance, including correcting the gravity data for known anomalous crustal density structures, mainly density variations of oceans, glacial ice, and sediments (i.e. stripping gravity corrections). For this purpose, the gravimetric forward modelling approach is used to compute the stripping gravity corrections using the ESCM180 Earth's spectral crustal model, which was derived based on refining the CRUST1.0 global crustal model (*cf.* Tenzer et al. 2009, 2010, 2012c, 2015). Moreover, gravity signals associated with deeper masses below the crust (i.e. non-isostatic effects) must also be taken into account. To do so, we use the method presented by Bagherbandi & Sjöberg (2012) to estimate the non-isostatic correction/effect (NIE) on gravity using the recent seismic crustal thickness in CRUST19 model by comparing the gravimetric and seismic data in the frequency domain. CRUST19 is a global crustal model based on a USGS database of crustal seismic studies. CRUST19 was also used to obtain the MD (D_0) and the NIE.

3.2 Validation of CRUST1.0 model versus CRUST2.0 model

As we will partly rely on CRUST1.0 model for our application, we start to compare it with CRUST2.0. First, it should be noted that the resolution of CRUST1.0 is $1^\circ \times 1^\circ$, while that for CRUST2.0 is $2^\circ \times 2^\circ$. CRUST2.0 is an updated version of the CRUST5.1 model (Mooney *et al.* 1998), it incorporates 360 key crustal types that contain the thickness, density and velocity of compressional (V_p) and shear waves (V_s) for seven layers (ice, water, soft sediments, hard sediments, upper, middle and lower crust). The V_p values are based on field measurements, while V_s and density are estimated by using empirical V_p–V_s and V_p–density relationships, respectively. In 2013, CRUST2.0 was updated to CRUST1.0. Apart from the higher resolution CRUST1.0 is based on ETOPO1 for topography and bathymetry, sediment basins are taken from a $1^\circ \times 1^\circ$ model (Laske & Masters 1997), while the crustal thickness is a compilation of active source experiments, receiver functions and already published Moho maps.

(1) The first step of the comparison is to compute the difference between the two models, $M^{(1)}_{i,j}$ and $M^{(2)}_{i,j}$, for each grid cell (i, j)as

$$\delta M_{i,j} = M^{(1)}_{i,j} - M^{(2)}_{i,j}, \tag{9a}$$

where $M^{(1)}_{i,j}$ and $M^{(2)}_{i,j}$ are assumed to be the CRUST1.0 and CRUST2.0 models. We then consider a statistical test, which shows how well $M^{(1)}_{i,j}$ is statistically related to $M^{(2)}_{i,j}$. Therefore, we define a null hypothesis (H_0) and an alternative hypothesis (H_a) as follows:

$$\begin{cases} H_0 : \eta^{(1)}_{i,j} = \eta^{(2)}_{i,j} \\ H_\mathrm{a} : \eta^{(1)}_{i,j} \neq \eta^{(2)}_{i,j} \end{cases}, \tag{9b}$$

where $\eta^{(1)}_{i,j}$ and $\eta^{(2)}_{i,j}$ are the expected values of the models.

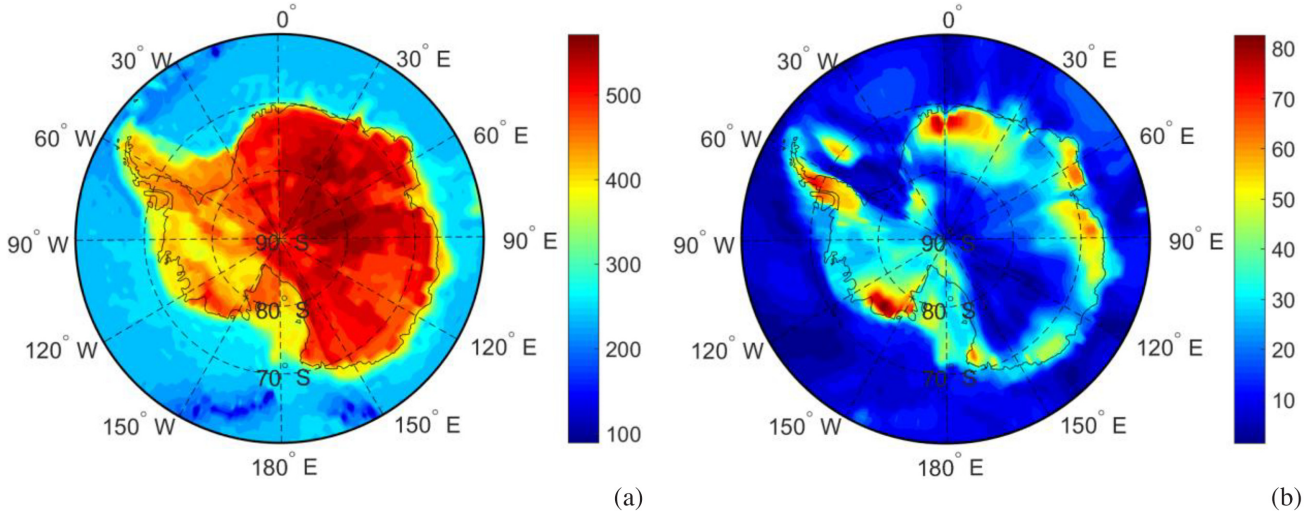

Figure 4. (a) The MDC estimated by HVMDC20 and (b) its estimated STE (in kg m^{-3}).

Table 3. Source of MDC models used in this study.

Model ID	Resolution	Model description
KTH11 (Sjöberg & Bagherbandi 2011)	2° × 2°	Gravimetric Moho model derived from CRUST2.0 and EGM2008 data
GEMMA12C (Reguzzoni *et al.* 2013)	2° × 2°	Combined model of CRUST2.0 and GOCE data
CRUST1.0 (Laske *et al.* 2013)	1° × 1°	Global crustal model derived from seismic data
KTH15C (Abrehdary *et al.* 2017)	1° × 1°	Combined model of CRUST1.0 and GOCO05S data

Table 4. Statistics of the differences between the HVMDC20 and other global models. STD is the standard deviation. RMS is root mean square. KTH11, GEMMA12C and KTH15C are the MDCs used to compare with those from HVMDC20.

Unit	Quantities	Max.	Mean	Min.	STD	RMS
kg m^{-3}	HVMDC20–KTH11	294.87	115.92	-148.15	59.35	130.23
	HVMDC20–GEMMA12C	411.32	187.47	-51.11	97.32	211.22
	HVMDC20–CRUST1.0	131.57	-21.52	-195.36	56.82	60.76
	HVMDC20–KTH15C	176.71	-13.06	-141.63	49.15	50.86

The test parameter, which is approximately t-distributed, is given by

$$t_{\text{obs}} = \frac{M_{i,j}^{(1)} - M_{i,j}^{(2)}}{S_{(\bar{M}_{i,j}^{(1)} - \bar{M}_{i,j}^{(2)})}}, \tag{9c}$$

where $S_{(\bar{M}_{i,j}^{(1)} - \bar{M}_{i,j}^{(2)})}$ is the standard error of the mean difference between the models.

The standard errors in the CRUST1.0 and CRUST2.0 models are defined empirically, implying 5 and 10 per cent of the calculated depth of the Moho as stated in Christensen & Mooney (1995).

For a given confidence level of $1-\alpha$ (α chosen as 0.05) and degree of freedom, df, the null hypothesis is met for

$$-t_{\frac{\alpha}{2},\text{df}} \leq t_{\text{obs}} \leq t_{\frac{\alpha}{2},\text{df}}, \tag{9d}$$

where $t_{\frac{\alpha}{2},\text{df}}$ is the critical value in the upper and lower tail of the t-distribution, and otherwise H_a holds.

The MDs of the considered models are shown in Figs 1(a) and (b).

Generally, one can point out that the main differences between CRUST2.0 and CRUST1.0 are in the number of crustal types that decreases from 360 to 35, in the change of the upper mantle density model and in the introduction of mid oceanic ridges. In Fig. 1(c) one can observe that main differences between CRUST2.0 and CRUST1.0 MDs in Ross ice shelf and Marie Byrd land are of the order of −15.9 km in mean value with a standard deviation of 4 km, partially due to the different resolutions and partially due to the different data set. Other differences between two models are located mainly in the areas of transition between continental and oceanic crust and in the presence of young oceanic crust (see also Sampietro *et al.* 2013).

Fig. 1(d) plots the coherence between CRUST1.0 and CRUST2.0 MD, which follows from eq. (9d). The major advantage of using this plot is that it easily allows to detect the presence of anomalies in the crust (e.g. subduction, duplication and fragmentation of the crust). In the figure yellow areas indicate that the null hypothesis in eq. (9d) is rejected, implying that the two models are not consistent. This result may have two causes: either that the two estimated MD differ or that the estimated model accuracy is wrong, or both. With reference to Figs 1(a)–(d) one can see that CRUST1.0 agree to 4 km in RMS with CRUST2.0, in 88 per cent of the area.

(1) We also present the scatter plots between CRUST1.0 and CRUST2.0 models to evaluate CRUST1.0 versus the other model. Scatter plots can usually be used to identify relationship between models.

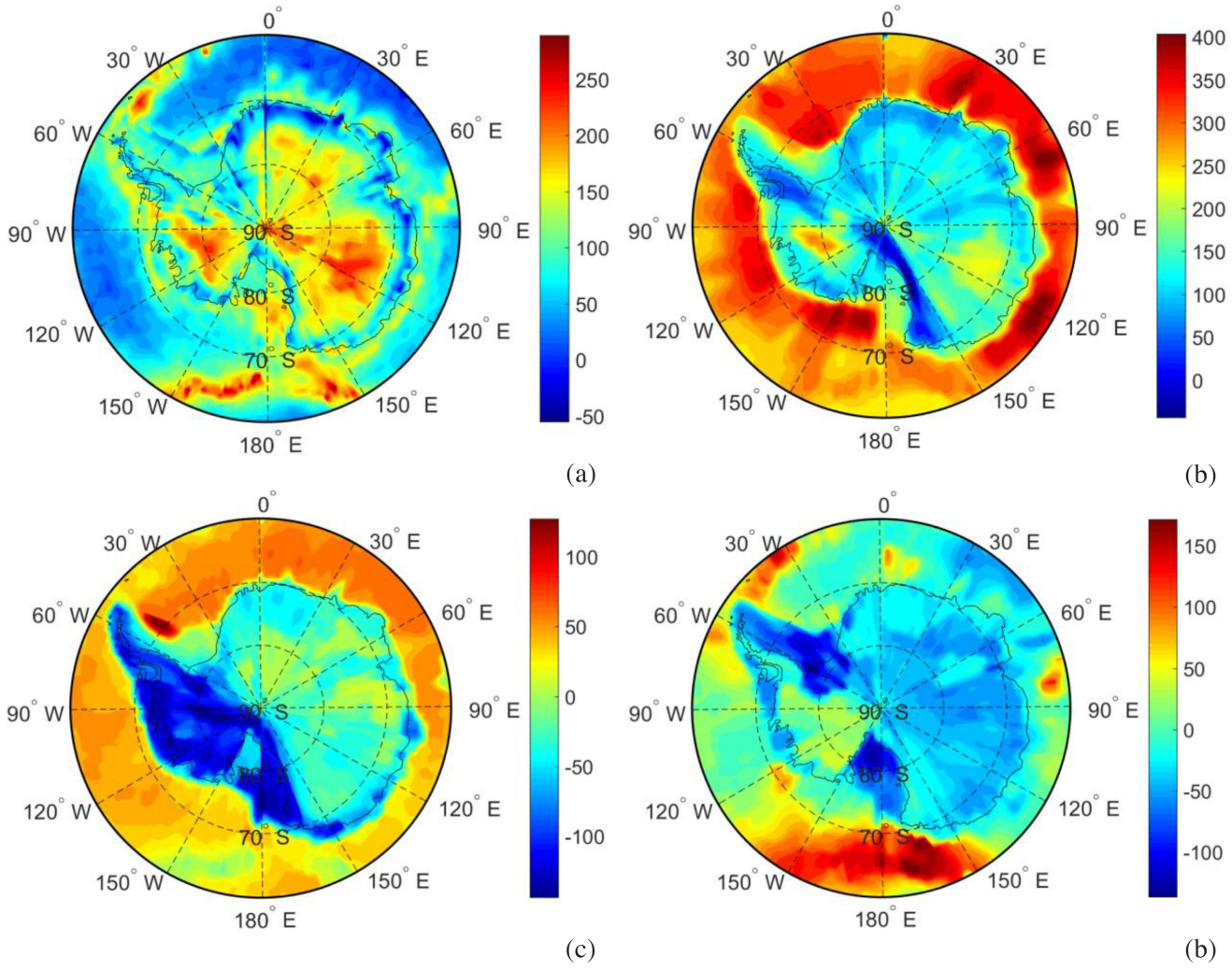

Figure 5. The differences between HVMDC20 and MDCs from (a) KTH11, (b) GEMMA12C, (c) CRUST1.0 and (d) KTH15C model (in kg m^{-3}).

Fig. 2 depicts scatter plots of the global MD models CRUST1.0 versus CRUST2.0. As can be seen, in order to figure out the relationship between pairs of the models, a line that best fits all the data (or regression line) has been performed (i.e. red middle line). The two additional lines (i.e. top and bottom lines) are drawn as ± twice of RMS differences between the models (i.e. fitted line ± 2 RMS differences) to assess the variation between the two models. Note the general linear correlation of the models in the plot indicating the overall agreement. One can also see outliers (i.e. plots outside the outer lines), which might be attributed to the improvements considered in CRUST1.0.

The validation of the global Moho models of CRUST1.0/CRUST2.0 is not an easy task due to the small amount of direct observations, (e.g. from seismic techniques) and to their limited accuracy, but nevertheless according to our validations, it is concluded that CRUST2.0 is a comparatively poor model for Antarctica (see also Abrehdary *et al.* 2017).

Table 1 shows some statistics of the free-air and refined Bouguer gravity disturbances and corrections, and more details on these disturbances are visualized in Figs 3(a)–(g). Fig. 3(a) depicts that the Antarctic free-air gravity disturbances differ mostly within ±80 mGal, with the largest values over the Antarctic Peninsula and large parts of East Antarctica, and small values mainly over the West Antarctic Rift System and the Transantarctic Mountains. The resulting refined Bouguer disturbance vary between 5.8 and 424.5 mGal on the continent and between −585.9 and −21.3 mGal on the surrounding seas (Fig. 3g). As can be seen from Figs 3(a) and 3(g), these corrections significantly change the Bouguer gravity disturbance from the free-air disturbance over oceans due to the application of the bathymetric stripping gravity correction (Fig. 3c), and in continental Antarctica due to application of the ice density variation stripping gravity correction (Fig. 3d), and the change is less remarkable when applying the sediment density variation stripping gravity correction (Fig. 3e). Notable is also the large NIE in some ocean areas. The most pronounced effect of the NIE due to remaining GIA is naturally found in areas with the highest post-glacial rebound (*cf.* Section 5).

3.3 The variable Moho density contrast and its uncertainty

Table 2 summarizes some statistics of the MDC of HVMDC20 and its STE estimated by eq. (8), and details are shown in Figs 4(a) and (b). The MDC varies between 81 kg m^{-3} in some remote areas of the open sea to high values in the NE of the continent, reaching 579 kg m^{-3} in central Antarctica (in the Gamburtsev Mountain Range), and its STE is generally below 50 kg m^{-3}, varying between

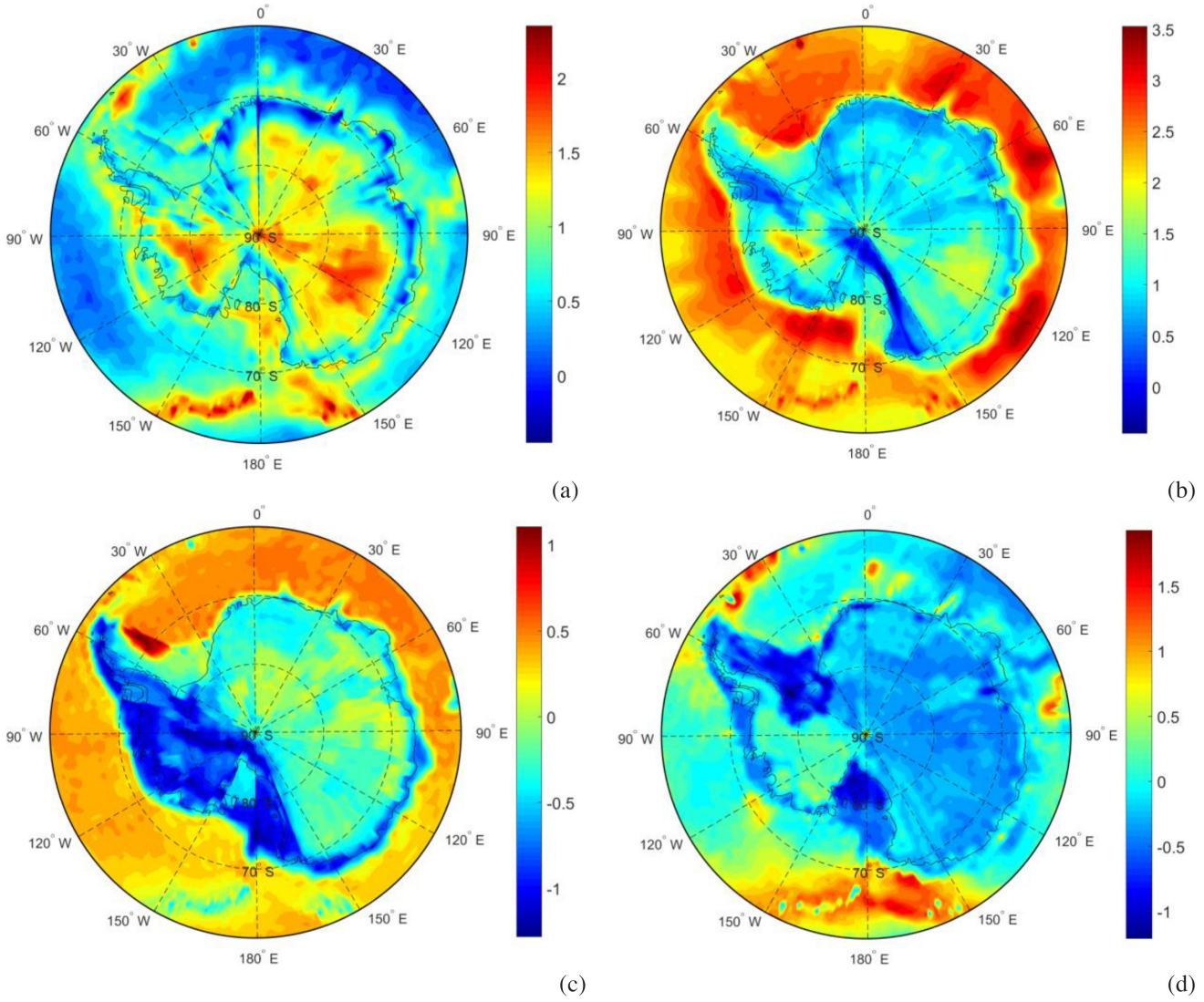

Figure 6. The differences between HVMDC20 MDC and those from (a) KTH11, (b) GEMMA12C, (c) CRUST1.0 and (d) KTH15C model divided by the standard deviation of our HVMDC20 model.

0.28 and 84 kg m^{-3}. The smallest STEs are seen in the ocean but also in some continental areas, and the largest values can be found in some coastal areas.

Fig. 4(a) maps the MDCs produced by HVMDC20 in Antarctica and surrounding seas. As can be observed in the figure, the MDCs differ significantly in East and West Antarctica with a maximum of about 580 kg m^{-3} located in the central part of the continent. Smaller MDCs, typically less than 300 kg m^{-3}, are seen in the oceanic areas.

Fig. 4(b) images the STE of HVMDC20 estimated by eq. (8). From the figure one can observe that most of the STDs are less than 50 kg m^{-3}, but they reach to more significant values (up to 80 kg m^{-3}) in some regions.

3.4 HVMDC20 assessment

Here we compare our results with those from the models KTH11, GEMMA12C, CRUST1.0 and KTH15C. Table 3 lists some properties of the models used in the comparison, and Table 4 shows the statistics of the comparisons of the MDCs with HVMDC20. Details of comparisons are shown in Figs 5(a)–(d).

Fig. 5(a) displays that HVMDC20 is not in good agreement with model KTH11, which could be explained by that neither the density variations related to the Earth crust, nor those related to the upper mantle were considered in KTH11, leading to an underestimation of the MDC (Abrehdary *et al.* 2017), which seems to be more realistic in the HVMDC20 model.

Fig. (5b) demonstrates that HVMDC20 and GEMMA12C are inconsistent in the ocean regions, while the agreement is acceptable on the continent. The discrepancies in the Antarctic seas could be attributed to the use of the generally inferior CRUST2.0 in the GEMMA12C and also to the differences in data resolution, and weighting of the different contributions (Reguzzoni *et al.* 2013).

Fig. 5(c) illustrates that the HVMDC20 agrees fairly well with CRUST1.0. The largest disagreements, of the order of 100 kg m^{-3} are found in the SE of the continent and in a small ocean area to the NW. These deviations may be attributed to the constraints used in

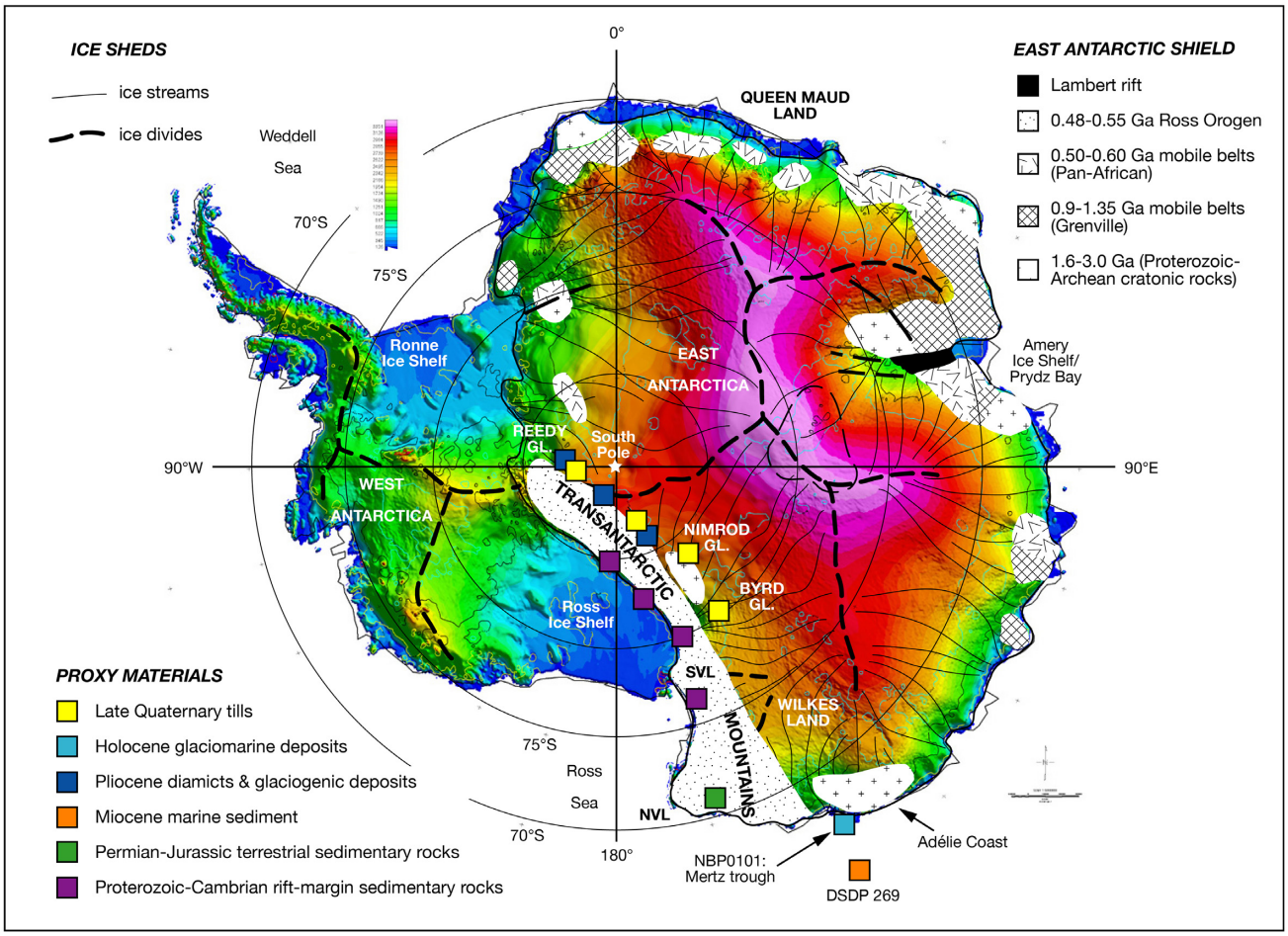

Figure 7. Map of Antarctica showing elevations of East and West Antarctic ice caps (Lythe *et al.* 2001), principal East Antarctic shield geology (after Fitzsimons 2000), modern glacial flow (after Barker *et al.* 1998) and study areas used for sampling of sedimentary and glacially transported proxies. Warmer colours indicate higher ice surface elevations (Goodge 2007).

Table 5. Statistics of the GIA gravity and its effects on the MDC over Antarctica. STD is the standard deviation of the estimated quantities over the ocean blocks. δg^{GIA} and $\Delta\rho^{\mathrm{GIA}}$ are the GIA effects on gravity and MDC, respectively.

Unit	Quantities	Max.	Mean	Min.	STD
kg m^{-3}	$\Delta\rho^{\mathrm{GIA}}$	14.41	−0.28	−13.01	5.88
mGal	δg^{GIA}	20.54	−1.37	−18.55	6.79

the CRUST1.0, which gives little information on Antarctic interior (Llubes *et al.* 2018).

In Fig. 5(d), one can observe that although the KTH15C model shows a very good agreement with ours, however, some disagreements are found in some regions, which may be due to using erroneous prior information in the KTH15C and/or imperfect estimates in HVMDC20 in these areas.

In Fig. 6, the differences between HVMDC20 and MDCs from (a) KTH11, (b) GEMMA12C, (c) CRUST1.0 and (d) KTH15C model divided by the standard deviation of our HVMDC20 model are plotted, which can help us to localize specific regions, where the disagreements with KTH11, GEMMA12C, CRUST1.0 and KTH15C are bigger than $\pm 1\sigma$. As can be seen from Fig. 6(a), HVMDC20 agree rather poor with KTH11, which could be attributed on one hand to density variations related to the Earth crust and those related to the upper mantle were not considered in KTH11, which probably led to an underestimation of the MDC, that seems to be more realistic in the HVMDC20 model. Another problem was the use of the inferior CRUST2.0 model in KTH11 (but CRUST1.0 in HVMDC20), as the difference between the CRUST2.0 and CRUST1.0 is significant as shown in Figs 1(a)–(d). Fig. 6(b) shows that HVMDC20 and GEMMA12C are not in good consistency, which again can partly be explained by the utilizing the CRUST2.0 model in GEMMA12C and also to the differences in data resolution. Figs 6(c) and (d) reveal that HVMDC20 is compatible with two models (CRUST1.0 and KTH15C), and in most areas the agreements are within $\pm 1\sigma$. However, in some regions they disagree significantly, which may be due to erroneous prior information in KTH15C and CRUST1.0 uncertainties in these areas.

4 BRIEF OVERVIEW OF HVMDC20 IN ANTARCTICA

In order to better assess the MDC modelling by HVMDC20, we employ the thematic map plotted in Fig. 7, which shows elevations of East and West Antarctic ice caps, principal East Antarctic shield geology, modern glacial flow, and study areas used for sampling of sedimentary- and glacially transported proxies.

Fig. 4(a) shows that small MDCs, less than 150 kg m^{-3}, are found in ocean areas, which is obviously due to the thinning of the

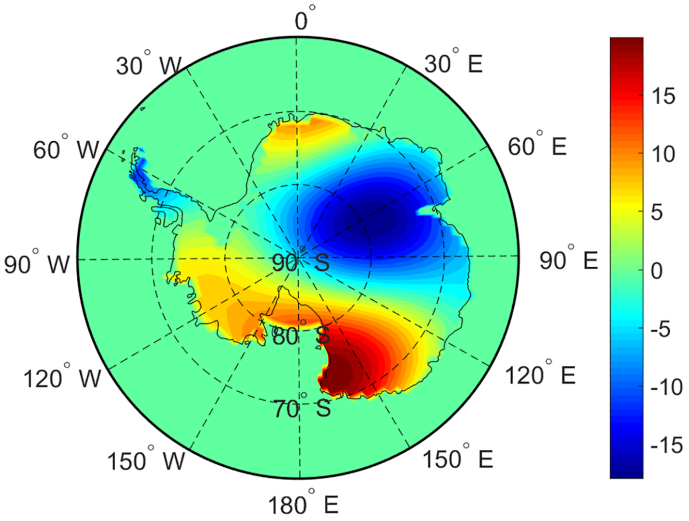

Figure 8. The GIA effect on gravity with spectral window $7 \leq n \leq 12$ (unit: mGal).

oceanic crust, particularly along the Pacific Antarctic mid-oceanic ridge. As can also be seen from Fig. 4(a), the MDCs change significantly between East and West Antarctica, with higher values in the East, particularly under the Gamburtsev Subglacial Mountains, confirming the presence of deep and compact orogenic roots. Comparing with Fig. 7, one can see that the MDCs are fairly notable in East Antarctica under Dronning Maud Land with two orogenic roots under Wohlthat Massif and the Kottas Mountains, that are separated by a relatively thin crust along Jutulstraumen Rift (see also Baranov *et al.* 2018). Large MDCs in East Antarctica, exceeding 500 kg m^{-3}, are accumulated throughout the central part, which is even extended under the Transantarctic Mountains. This is because, apart from small areas along the coast, East Antarctica is permanently covered by ice. The MDC in West Antarctica is also significant but less pronounced than that in the Eastern counterpart. Especially in SW Antarctica the MDC is typically 400–450 kg m^{-3}, which is attributed to the presence of the West Antarctic Rift system, extending over a 3000 × 750 km^2, with large ice-covered areas from the Ross Sea to the base of the Antarctic Peninsula. The MDCs observed under the mountain ranges and areas covered by the largest continental ice sheet are also significant.

5 GLACIAL ISOSTATIC ADJUSTMENT (GIA) OVER ANTARCTICA

This section models the remaining glacial isostatic adjustment (GIA) effect on gravity to figure out how this affects MDC determination. GIA is the ongoing movement of land once loaded by ice-age glaciers. The process of GIA refers to isostatic deformation related to ice and water loading during a glacial cycle. Isostasy involves adjustment of the crust responding to the mass transport across its surface (Watts 2001, p.48), implying that the crust forms in response to the gravitational effect of dynamic processes due to GIA. Usually, the GIA effect is part of the NIEs, and the observed gravity disturbances are already corrected for it, but here we investigate specifically the GIA impact for Antarctica to figure out how much of the GIA signal can affect the MDC determination. To achieve this, we use the spherical harmonic spectral window 7–12 of the gravity field, which yields the largest correlation coefficient (∼0.60) with the GIA model W12a (Whitehouse *et al.* 2012). Applying this spectral window to the gravity disturbance and MDC (based on the VMM technique) is visualized in Table 5 and Fig. 8, respectively.

The remaining GIA is a non-isostatic gravity signal, which will falsely affect the MDC results if not considered. However, with reference to Table 2 and Fig. 8, one can see that the GIA effect on gravity (6.7 mGal in the STD) and on MDC (5.8 kg m^{-3} in the STD) versus the STD of the estimated MDCs (123 kg m^{-3}) are not significant. Consequently, we conclude that the remaining GIA has no significant effect on the estimated MDC over Antarctica.

6 CONCLUSIONS

The VMM technique has been applied successfully in the new MDC model HVMDC20 with a resolution of 1° × 1° in Antarctica and surrounding seas using the recent gravity field model XGM2019e and Earth2014 topographic/bathymetric information along with CRUST1.0 and CRUST19. The model is also attached with a map of its estimated STE, (but possible significant systematic errors are missing). The STE of the oceanic MDC is typically 10 kg m^{-3} or less, while on the continent it reaches more than 80 kg m^{-3} at some places.

To validate the results, we have compared HVMDC20 with the similar models KTH11, GEMMA12C, CRUST1.0 and KTH15C, showing that the last two models agree well with HVMDC20. In addition, we have studied the signatures of geological unit structures in HVMDC20, showing how the main geological and ice sheet structures attribute in the MDC. Finally, we have specifically investigated the remaining GIA effect on gravity to figure out how it affects MDC recovery, yielding a correlation of the order of ∼0.6 with the W12a GIA model and contributing within ±14 kg m^{-3} to the MDC.

ACKNOWLEDGEMENTS

This study was supported by project no. 187/18 of the Swedish National Space Agency (SNSA). Prof. John Goodge from the University of Minnesota is acknowledged for providing the geology map of Antarctica.

REFERENCES

Abrehdary, M., Sjöberg, L.E. & Bagherbandi, M., 2015. Modelling Moho depth in ocean areas based on satellite altimetry using Vening Meinesz–Moritz' method, *Acta Geod. Geophys.,* **51**(2), 137–149.

Abrehdary, M., Sjöberg, L.E., Bagherbandi, M. & Sampietro, D., 2017. Towards the Moho depth and Moho density contrast along with their uncertainties from seismic and satellite gravity observations, *J. Appl. Geod.,* **11**(4), 231–247.

Abrehdary, M., Sjöberg, L.E. & Sampietro, D., 2019. Contribution of satellite altimetry in modelling Moho density contrast in oceanic areas, *J. Appl. Geod.,* **13**(1), 33–40.

Bagherbandi, M. & Sjöberg, L.E., 2012. Non-isostatic effects on crustal thickness: a study using CRUST2. 0 in Fennoscandia. *Phys. Earth planet. Inter.,* **200,** 37–44.

Baranov, A., Tenzer, R. & Bagherbandi, M., 2018. Combined gravimetric–seismic crustal model for Antarctica. *Surv. Geophys.,* **39**(1), 23–56.

Barker, P.F. *et al.*, 1998. Ice sheet history from Antarctic continental margin sediments: the ANTOSTRAT approach, *Terra Antarctica,* **5,** 737–760.

Bassin, C., Laske, G. & Masters, G., 2000. The current limits of resolution for surface wave tomography in North America, *EOS, Trans. Am. geophys. Un.,* **81,** F897.

Christensen, N.I. & Mooney, W.D., 1995. Seismic velocity structure and composition of the continental crust: A global view, *Journal of Geophysical Research: Solid Earth,* **100**(B6), 9761–9788.

Eshagh, M., 2017. On the approximations in formulation of the Vening Meinesz–Moritz theory of isostasy, *Geophys. J. Int.,* **210**(1), 500–508.

Fitzsimons, I.C.W., 2000. A review of tectonic events in the East Antarctic Shield, and their implications for Gondwana and earlier supercontinents, *J. Afr. Earth Sci.,* **31,** 3–23.

Goodge, J.W., 2007, Proxies of the East Antarctic shield: composition and age of ice-covered basement from sedimentary and glacial provenance, in *Antarctica: a Keystone in a Changing World—Online Proceedings of the 10th International Symposium on Antarctic Earth Sciences,* US Geological SurveyOpen-File Report 2007-1047, Extended Abstract 132, 4 p.

Haeger, C., Kaban, M.K., Tesauro, M., Petrunin, A.G. & Mooney, W.D., 2019. 3-D density, thermal, and compositional model of the Antarctic lithosphere and implications for its evolution, *Geochem. Geophys. Geosyst.,* **20**(2), 688–707.

Heiskanen, W.A. & Moritz, H., 1967, *Physical Geodesy*. W. H. Freeman.

Hirt, C. & Rexer, M., 2015. Earth2014: 1 arc-min shape, topography, bedrock and ice-sheet models—available as gridded data and degree-10,800 spherical harmonics, *Int. J. Appl. Earth Obs. Geoinf.,* **39,** 103–112.

Laske, G. & Masters, G., 1997. A global digital map of sediment thickness, *EOS, Trans. Am. geophys. Un.,* **78,** F483.

Laske, G., Masters, G., Ma, Z. & Pasyanos, M.E., 2013. A New Global Crustal Model at 1x1 Degrees (CRUST1.0), http://igppweb.ucsd.edu/~gabi/crust1.html.

Llubes, M., Seoane, L., Bruinsma, S. & Rémy, F., 2018. Crustal thickness of Antarctica estimated using data from gravimetric satellites, *Solid Earth,* **9**(2), 457.

Lythe, M.B. *et al.*, 2001. BEDMAP; a new ice thickness and subglacial topographic model of Antarctica, *J. geophys. Res.,* **106,** 11 335–11 351.

Mooney, W.D., Laske, G. & Masters, T.G., 1998. CRUST 5.1: a global crustal model at 5°x5°, *J. geophys. Res.,* **103**(B1), 727–747.

Pappa, F., Ebbing, J. & Ferraccioli, F., 2019a. Moho depths of Antarctica: comparison of seismic, gravity, and isostatic results, *Geochem. Geophys. Geosyst.,* **20**(3), 1629–1645.

Pappa, F., Ebbing, J., Ferraccioli, F. & van der Wal, W., 2019b. Modeling satellite gravity gradient data to derive density, temperature, and viscosity structure of the Antarctic lithosphere, *J. geophys. Res.,* **124**(11), 12 053–12 076.

Reguzzoni, M., Sampietro, D. & Sansò, F., 2013. Global Moho from the combination of the CRUST2. 0 model and GOCE data, *Geophys. J. Int.,* **195,** 222–237.

Sampietro, D., Reguzzoni, M. & Negretti, M., 2013. The GEMMA crustal model: first validation and data distribution. *ESA Special Publication,* **722,** 30.

Sjöberg, L.E., 2009, Solving Vening Meinesz-Moritz inverse problem in isostasy, *Geophys. J. Int.,* **179**(3), 1527–1536.

Sjöberg, L.E., 2013, On the isostatic gravity disturbance and disturbance and their applications to Vening Meinesz–Moritz gravimetric inverse problem, *Geophys. J. Int.,* **193**(3), 1277–1282.

Sjöberg, L.E. & Bagherbandi, M., 2011. A method of estimating the Moho density contrast with a tentative application of EGM08 and CRUST2. 0, *Acta Geophys.,* **59**(3), 502–525.

Szwillus, W., Afonso, J.C., Ebbing, J. & Mooney, W.D., 2019. Global crustal thickness and velocity structure from geostatistical analysis of seismic data, *J. geophys. Res.,* **124**(2), 1626–1652.

Tenzer, R., Abdalla, A., Vajda, P. &Hamayun, 2010. The spherical harmonic representation of the gravitational field quantities generated by the ice density contrast, *Contrib. Geophys. Geod.,* **40**(3), 207–223.

Tenzer, R. & Bagherbandi, M., 2013. Reference crust-mantle density contrast beneath Antarctica based on the Vening Meinesz-Moritz isostatic inverse problem and CRUST2.0 seismic model, *Earth Sci. Res. J.,* **17**(1), 7–12.

Tenzer, R., Bagherbandi, M. & Gladkikh, V., 2012b. Signature of the upper mantle density structure in the refined gravity data, *Comput. Geosci.,* **16**(4), 975–986.

Tenzer, R., Bagherbandi, M. & Vajda, P., 2013. Global model of the upper mantle lateral density structure based on combining seismic and isostatic models, *Geosci. J.,* **17**(1), 65–73.

Tenzer, R., Chen, W., Tsoulis, D., Bagherbandi, M., Sjöberg, L.E., Novák, P. & Jin, S., 2015. Analysis of the refined CRUST1.0 crustal model and its gravity field, *Surv. Geophys.,* **36**(1), 139–165.

Tenzer, R., Hamayun, K. & Vajda, P., 2009. Global maps of the CRUST2.0 crustal components stripped gravity disturbances, *J. geophys. Res.,* **114**(B5), doi:10.1029/2008JB006016.

Tenzer, R., Novák, P., Gladkikh, V. & Vajda, P., 2012a. Global crust-mantle density contrast estimated from EGM2008, DTM2008, CRUST2. 0, and ICE-5G, *Pure appl. Geophys.,* **169**(9), 1663–1678.

Tenzer, R., Novák, P., Vajda, P., Gladkikh, V. &Hamayun, 2012c. Spectral harmonic analysis and synthesis of Earth's crust gravity field, *Comput. Geosci.,* **16**(1), 193–207

Watts, A.B., 2001, *Isostasy and Flexure of the Lithosphere,* Cambridge Univ. Press, xix + 458 pp.

Whitehouse, P.L., Bentley, M.J., Milne, G.A., King, M.A. & Thomas, I.D., 2012. A new glacial isostatic adjustment model for Antarctica: calibrated and tested using observations of relative sea-level change and present-day uplift rates, *Geophys. J. Int.,* **190**(3), 1464–1482.

Zingerle, P., Pail, R., Gruber, T. & Oikonomidou, X., 2019. The experimental gravity field model XGM2019e, GFZ Data Services, doi:10.5880/ICGEM.2019.007.